https://doi.org/10.5194/egusphere-2025-4302
Preprint. Discussion started: 17 September 2025

Impact of small-scale orography on deep boundary layer evolution and structure over the Tibetan Plateau

Ivan Basic[1,2], Harshwardhan Jadhav[1,2], Jaydeep Singh[1,2], and Juerg Schmidli[1,2]

[1]Institute for Atmospheric and Environmental Sciences, Goethe University Frankfurt, Altenhöferallee 1, 60438 Frankfurt/Main, Germany
[2]Hans-Ertel Centre for Weather Research, Deutscher Wetterdienst, Frankfurter Straße 135, 63067 Offenbach, Germany

Correspondence: Ivan Basic (basic@iau.uni-frankfurt.de)

Abstract. We investigate how small-scale orography influences the evolution and structure of the exceptionally deep convective boundary layer (CBL) over the Tibetan Plateau (TiP). Using large-eddy simulations (LES) at 50 m resolution under semi-idealized dry conditions, we compare three experiments over an elevated plateau (4.2 km above sea level (ASL)): FLAT (no orography), REAL (realistic terrain), and REALu10 (REAL terrain plus a upper-level wind of 10 m s^{-1}). All simulations produce very deep CBL, reaching ∼9 km ASL by late afternoon, consistent with the record-high values observed over the TiP. Small-scale orography substantially accelerates early growth: by midday the CBL in REAL is ∼80 m higher than in FLAT, and locally above the mountain it is ∼500 m deeper. This terrain-induced advantage narrows later in the day as all cases attain extreme depths. In REALu10, the CBL grows even higher, reaching 9.4 km ASL by 19 LT. Added shear organizes convection into longitudinal roll vortices, contrasting with the isolated terrain-anchored plumes in the no-shear case, and enhances vertical mixing.

These results demonstrate that unresolved small-scale orography can increase daytime CBL height by up to 15% and expedite entrainment of free-tropospheric air. Under clear-sky conditions, the plateau's CBL can exceed 9 km within a single day given strong surface heating and weak stability aloft. Our findings highlight the importance of including fine-scale terrain and shear effects in models, as their omission may underestimate CBL growth and vertical exchange over high-altitude regions.

1 Introduction

The atmospheric boundary layer (ABL) over the TiP plays a crucial role in the climate system, regional weather, and air quality. Despite its importance, many aspects of the TiP's boundary layer remain poorly understood due to sparse observations over this remote high-altitude region (Che and Zhao, 2021). One distinguishing feature of the TiP's ABL is its extraordinary depth. Summertime CBLs commonly grow 2-4 km above ground level (AGL) across the plateau, far deeper than over lowland terrain. Even higher extremes have been observed under favorable conditions. In winter and spring, for example, ABL heights of 9 km ASL have been recorded (Chen et al., 2013), effectively bringing the boundary layer into contact with the tropopause and enabling exchange of air between the surface and lower stratosphere (Chen et al., 2016). Such deep vertical mixing has important implications for atmospheric composition: the TiP is a global hotspot for stratospheric intrusions, which can elevate

https://doi.org/10.5194/egusphere-2025-4302
Preprint. Discussion started: 17 September 2025

surface ozone and other tracer gases over the plateau (Yin et al., 2023; Ojha et al., 2017). These characteristics make the TiP ABL a unique and influential component of the Asian climate system.

Observational and modeling studies have begun to uncover the controls on the plateau's deep ABL and vigorous vertical mixing. The intense sensible heat flux from the heated surface creates strong convective turbulence, allowing the ABL to grow to great heights (Zhao et al., 2023). In dry and cloud-free regions, this effect is especially pronounced, as more incoming solar radiation is converted into turbulent heat flux (Zhang et al., 2011). Accordingly, the western and central TiP – characterized by low soil moisture, sparse cloud cover, and large sensible heat fluxes – tend to develop deeper daytime ABLs than the wetter eastern plateau (Che and Zhao, 2021; Santanello et al., 2005). Moisture availability also modulates boundary ayer growth in complex ways: when the surface is too dry, limited moisture constrains convection; when it's too wet, early cloud formation can reduce solar heating and inhibit further growth. (Xu et al., 2021). High-resolution simulations have shown that there is often an optimal intermediate soil moisture that produces the most vigorous convective development in the TiP's landscape (Gerken et al., 2015). In addition to forementioned factors, atmospheric stratification aloft also plays a crucial role: a weakly stable free atmosphere permits thermals to rise higher before stopping. Indeed, the extremely deep springtime ABLs observed over the plateau have been attributed to weak stability in the lower troposphere (Chen et al., 2016), rather than surface conditions alone. In summary, the ABL depth over the TiP is governed by a combination of intense surface heating, moisture availability, cloud feedbacks, and the thermal structure of the atmosphere above.

Accurately representing meteorology and ABL processes in mountainous terrain remains a major challenge for numerical weather and climate models. The ABL over complex orography is influenced by processes across multiple scales, from thermally driven slope and valley winds to mountain-wave breaking, heterogeneous turbulence, and land–atmosphere interactions (Lehner and Rotach, 2018; Serafin et al., 2018). Field studies further illustrate how local orography interacts with regional flow: along the eastern margin of the plateau, the interaction of plateau orography with regional circulations produces a regular alternation of low-level wind directions that governs weather in the adjacent Sichuan Basin (Li and Gao, 2007). Similarly, a Himalayan valley study showed that the alignment of synoptic winds with valley geometry dramatically affected ABL growth, with strong along-valley westerlies promoting deep (9 km ASL) mixing layers, while weaker cross-valley winds led to a much shallower ABL despite comparable surface heating (Lai et al., 2021). These examples demonstrate that orography can exert a first-order control on ABL depth and structure.

Yet the specific contribution of *smaller-scale* terrain features to the plateau's deep convective boundary layer remains poorly quantified. Most modeling studies have emphasized regional-scale influences while treating the terrain in smoothed or idealized form. However, even modest heterogeneities such as land–lake thermal contrasts can drive secondary circulations that alter turbulence and vertical transport (Zhang et al., 2021). Despite advances toward convection-permitting and cloud-resolving resolutions, models continue to face difficulties in capturing boundary-layer dynamics across scales (Solanki et al., 2019; Rajput et al., 2022; Singh et al., 2016; Guo et al., 2021). For example, Wagner et al. (2014) demonstrated in an idealized valley that unresolved terrain, rather than turbulence alone, can strongly alter ABL structure as resolution coarsens. Likewise, even LES at $\mathcal{O}$(100-300 m) resolution can suffer scale-transition issues, with excessive or insufficient turbulent mixing depending on the scheme used (Poll et al., 2022; Goger et al., 2022; Singh et al., 2021). Intercomparison studies further confirm that no

https://doi.org/10.5194/egusphere-2025-4302
Preprint. Discussion started: 17 September 2025

single ABL parameterization performs optimally across all conditions, underscoring the need for systematic validation and development (Singh et al., 2024). Even modern high-resolution reanalyses face similar challenges: ERA5 (with ∼30 km grid spacing) captures the general diurnal cycle of the plateau's boundary layer but often underestimates the deepest observed ABL peaks (Slättberg et al., 2022). The scarcity of *in situ* observations in the plateau's remote interior, especially over the western TiP, further complicates efforts to determine how small-scale terrain modulates ABL growth and mixing (Che and Zhao, 2021). Consequently, the role of the myriad hills, ridges, and gentle slopes that characterize the plateau's surface in shaping vertical exchange remains an open question.

These challenges motivate the present work, which examines the role of small-scale, unresolved orography on ABL height using high-resolution simulations. Our study explicitly focuses on how sub-kilometer orography influences ABL evolution, a key aspect that remains underexplored but is critical for improving predictions in complex terrain. We employ a cloud-resolving LES model, to perform semi-idealized, high-resolution simulations of daytime boundary layer evolution over a representative region of the TiP. Three simulation scenarios are compared: FLAT (no orography), REAL (realistic terrain), and REALu10 (REAL terrain plus steady upper-level wind of 10 m s^{-1}). Small-scale orography in this study refers to the REAL terrain, which features slopes up to 30° and ridge elevations reaching 1400 m within a 25×25 km domain. By analyzing these side-by-side experiments, we can directly assess how the presence of small-scale orography influences boundary layer dynamics. In addition, passive tracers are introduced into the model to serve as markers of air mass transport, mixing efficiency, and boundary layer height diagnosis. Comparing tracer dispersion and vertical profiles between the realistic terrain and flat terrain simulation provides a quantitative measure of terrain-induced enhancements (or suppressions) in vertical mixing. Through this approach, our study offers a clearer understanding of how small-scale orographic features contribute to the growth of the ABL and the vertical mixing processes over the TiP.

2 Methods

2.1 Numerical Model

The Cloud Model 1 (CM1) (Bryan and Fritsch, 2002) version 21.0 is utilized in LES mode. CM1 is an idealized, fully compressible, non-hydrostatic numerical atmospheric model with terrain-following coordinates. The simulations are conducted under dry conditions without any microphysics scheme, and latent heat fluxes are excluded. Subgrid-scale turbulence is parameterized by the 1.5-order TKE closure from Deardorff (1980).

Advection and momentum transport are handled by the Weighted Essentially Non-Oscillatory (WENO) scheme (Jiang and Shu, 1996), with improved smoothness indicators included (Borges et al., 2008). The scheme guarantees positive-definiteness and scalar mass conservation of passive tracers. For time integration, the Klemp-Wilhelmson time-splitting method (Klemp and Wilhelmson, 1978) is used, which keeps acoustic and gravity waves separated from the meteorologically relevant modes, thereby increasing computational efficiency.

The model domain is defined with a 50 m horizontal grid spacing and a size of 50 km×25 km×14 km, consisting of $500 \times 500 \times 216$ grid points. The vertical grid spacing is set to Δ20 m below 300 m altitude, then increases linearly from Δ20 m

https://doi.org/10.5194/egusphere-2025-4302
Preprint. Discussion started: 17 September 2025

to Δ100 m at 10 km, and then maintains constant spacing until 14 km. Previous studies have demonstrated that the CM1 model performs well for both idealized and semi-idealized setups when studying mountain-induced turbulence (Mulholland et al., 2021; Weinkaemmerer et al., 2022). The vertical grid spacing is set to 20 m below 300 m altitude, then increases linearly from 20 m at 30 m to a maximum of 100 m at 10 km, and maintains constant spacing of 100 m from 10 to 14 km. The model applies a semi-slip condition at the lower boundary and a free-slip condition for winds at the top boundary. The lateral boundary conditions are periodic representative of extensive mountainous terrain.

To simulate the high ABL of 9515 m ASL reported on March 4, 2008 (Chen et al., 2016), the model uses an idealized sounding as the initial condition: a 300 m surface mixed layer with constant potential temperature $\theta = 306.8$ K, followed by a stable layer with a weak lapse rate of 0.1 K/100 m until the top of the domain. A Rayleigh damping layer is introduced above 11.2 km altitude to the top of the model domain, with a damping time of 300 s. The Coriolis parameter is set to zero.

The surface exchange coefficients are constant, based on Monin-Obukhov similarity theory using a prescribed surface roughness length of 0.01 m. The diurnal cycle of surface sensible heat flux is prescribed as follows: starting at zero at 09 LT, it follows a sine function peaking at 180 W/m^2 after six hours (15 LT) and returning to zero after 11 hours (20 LT). These prescribed flux values are adopted based on the observed surface fluxes obtained from the authors of Chen et al. (2016).

To study mixing sources and to help in boundary layer height diagnosis, two passive tracers are introduced into the model. The first tracer is emitted as a constant surface flux $J_1 = 4 \times 10^{-5}$ kg/m^{2}s with no initial concentration ($c_{0,1} = 0$). The second tracer is initialized with a mixing ratio of $c_{0,2} = 1$ ppm above 4 km AGL and has no surface flux ($J_2 = 0$).

2.2 Experiments and Data

The study focuses on the Gerze station (32.178°N, 84.038°E) and its neighboring area (Fig. 1a,b), chosen to capture the influence of heterogeneous terrain, including nearby mountains ($\sim$ 1400 m), on the structure and evolution of the boundary layer. The actual orography was modified in two stages. First, the terrain near the domain edges (Fig. 1c) was tapered over a 4 km transition zone to 4200 m value, to satisfy periodic boundary conditions and maintain regional representativeness. Second, the tapered terrain was further smoothed with a Gaussian filter (200 m) to reduce extreme gradients, thereby preventing numerical instability of the model. Figure 1c shows the terrain for the REAL experiment with two subdomains: R-FLAT and R-TOPO, which are used in the analysis. Two additional experiments are defined as follows: FLAT, which represents the eleveated plateau at 4200 m ASL without small-scale orography, and REALu10, which is identical to REAL but includes a linear increase in wind speed above the mountain crest, reaching $u = 10$ ms^{-1}. The base elevation in both the FLAT case and along the smoothed edges of the REAL and REALu10 setup corresponds to the minimum elevation (4200 m) observed in the realistic terrain (Fig.1a). The experiments are summarized in Table 1. The terrain data is obtained from the Shuttle Radar orography Mission at approximately 30 m resolution (U.S. Geological Survey, 2015).

https://doi.org/10.5194/egusphere-2025-4302
Preprint. Discussion started: 17 September 2025

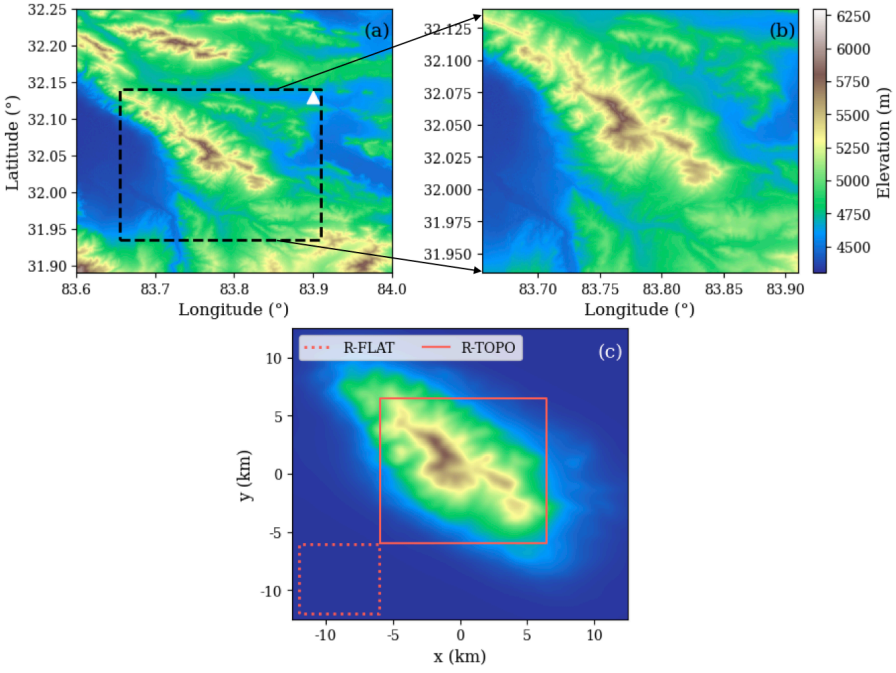

Figure 1. Terrain elevations shown as shaded relief. (a) Broader region centered near the Gerze station (white triangle) on the western Tibetan Plateau. (b) Zoomed-in view of the complex orography surrounding the area of interest, including nearby mountains and valleys. (c) Terrain height used in the REAL simulation, including the locations of the subdomains R-TOPO and R-FLAT used in the analysis. Elevation data is based on SRTM and reprojected to a Cartesian grid.

Table 1. List of the experiments and the subdomains. R-TOPO and R-FLAT refer to the subdomains depicted in Fig. 1c

Name	Description
FLAT	Flat orography
REAL	Real orography
REALu10	as REAL, but with u=10 m s^{-1} above the terrain
R-FLAT	Subdomain of REAL (4 km × 6 km)
R-TOPO	Subdomain of REAL (12.5 km × 12.5 km)

2.3 Analysis methods

2.3.1 Reynolds averaging and flow decomposition

One of the main advantages of the LES approach is its ability to explicitly resolve the large, energy-containing turbulent structures. As a result, the model output fields are inherently turbulent. It is therefore customary to decompose a turbulent flow

https://doi.org/10.5194/egusphere-2025-4302
Preprint. Discussion started: 17 September 2025

variable $a(\mathbf{x},t)$ into a mean and a fluctuating component:

$$a(\mathbf{x},t) = \overline{a}(\mathbf{x},t) + a'(\mathbf{x},t) \tag{1}$$

where $\overline{a}$ denotes the ensemble average and a' the turbulent fluctuation. In our study, this ensemble average is approximated by applying a two-dimensional Gaussian filter to the time-averaged variable $\tilde{a}^t$ such that

$$\overline{a}(x,y,z,t) = \int_A \tilde{a}^t(x',y',z,t) G(x-x',y-y') \tag{2}$$

where $G(x,y)$ is the two-dimensional Gaussian kernel.

This procedure was implemented by first performing online time-averaging of the instanteanous fields at 30 s intervals over 30 min time windows, yielding $\tilde{a}^t$ (cf. Weinkaemmerer et al., 2022). A two-dimensional Gaussian filter with a standard deviation of $\sigma = 500$ m and a cutoff radius of 4σ (resulting in a total support width of 4 km) was then applied using the `gaussian_filter` function from `scipy.ndimage`. Compared to pure time-averaging, this combined space-time filtering more effectively isolates turbulence-scale structures. The above flow decomposition is used consistently throughout the manuscript.

2.3.2 Diagnostic Boundary Layer Height via Tracer Method

To quantify the BL height, we apply a tracer-based diagnostic that captures the vertical extent of mixing and transport processes. The method identifies the BL height as the first vertical level z_i, where the smoothed tracer concentration $\phi(z)$ falls below 5% of the mean tracer concentration within the well-mixed layer, defined as: $\phi(z_i) \leq 0.05\overline{\phi}^{ML}$, where $\overline{\phi}^{ML}$ represents the average tracer concentration within the well-mixed portion of the boundary layer. To estimate $\overline{\phi}^{ML}$, a running mean is first applied to the tracer profile using a vertical window of two model levels, resulting in a smoothed profile defined on a new vertical coordinate $z_{h,\mathrm{win}}$. The lowest five model levels are excluded from this calculation to reduce the influence of the surface layer. Next, a cumulative mean of the tracer is computed at each point in the vertical and once the $\phi(z_i) \leq 0.05\overline{\phi}^{ML}$ condition is satisfied, the corresponding level is identified as the ABL height of the column. The first vertical level where the tracer concentration falls below this threshold is identified, and its corresponding height is defined as the diagnosed BL height. This method offers a dynamically adaptive and spatially consistent approach to detecting BL height, leveraging the tracer's ability to highlight regions influenced by turbulent mixing and vertical transport. To avoid a discretized ABL height, a linear interpolation between levels where $\phi(z_1) > \overline{\phi}^{ML}$ and $\phi(z_2) < \overline{\phi}^{ML}$ is applied.

3 Results

3.1 Mean Flow Evolution

Figure 2 shows the evolution of domain-averaged potential temperature and u-wind profiles. At 09 LT, the potential temperature profiles are nearly identical across all three experiments, confirming similar initial conditions. However, the domain-averaged

https://doi.org/10.5194/egusphere-2025-4302
Preprint. Discussion started: 17 September 2025

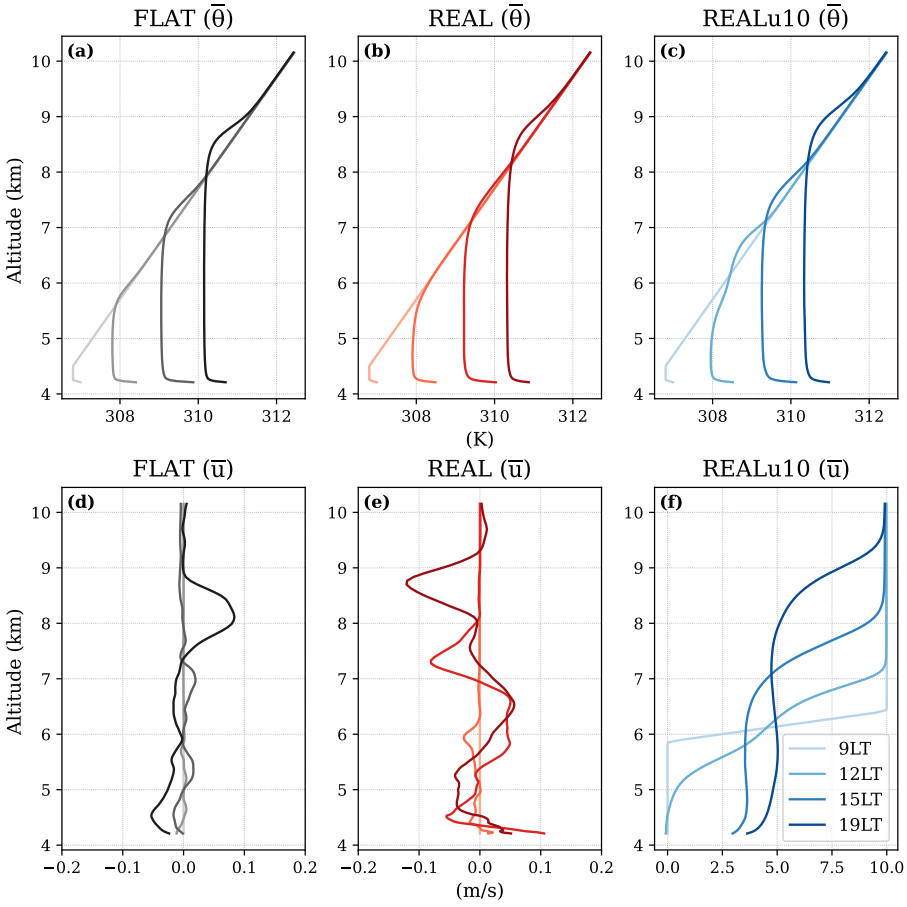

Figure 2. Diurnal evolition of the domain-averaged of potential temperature (top row) and u-wind component (bottom row), interpolated to horizontal surfaces.

profiles alone do not clearly capture structural differences in the CBL. To address this, Figure 3 depicts the spatial structure of convective activity at 15 LT, when the CBL is fully developed, showing the time-averaged vertical velocity and potential temperature fields, which reveal distinct patterns among the experiments. The spatial distribution of vertical velocity differs markedly between the FLAT and REAL terrain configurations due to underlying surface heterogeneity. In FLAT (Fig. 3a,d), cellular patterns are visible, updrafts (positive w) and downdrafts (negative w) are randomly distributed across the domain, reflecting the statistical homogeneity of the surface. Convective cells develop through turbulent interactions in the absence of fixed surface features, leading to temporally and spatially variable convective structures.

In contrast, the REAL terrain exhibits a distinctly organized vertical velocity field. Strong, localized updrafts are preferentially aligned with orographic features (see black contours in Fig. 3b, at 800 m), indicating convections' spatial stationarity. Elevated terrain serves as a main factor for differential surface heating, which generates persistent, thermally driven updrafts. This results in a more structured and spatially confined convective organization, with enhanced activity concentrated over and

https://doi.org/10.5194/egusphere-2025-4302
Preprint. Discussion started: 17 September 2025

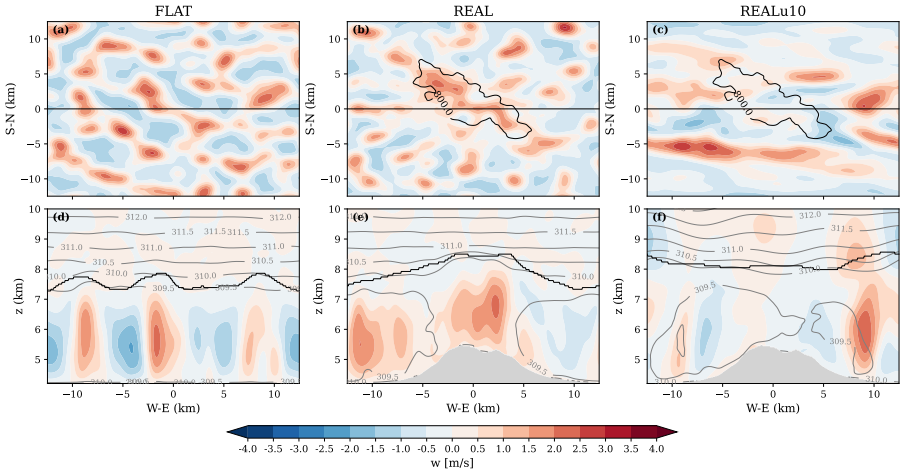

Figure 3. Snapshot of the ensemble average $\overline{w}$ for the different experiments at 15 LT. Top: horizontal cross-sections at 1800 m AGL (6 km ASL); bottom: vertical cross-sections at $y = 0$ with $\overline{\theta}$ (gray contours) and diagnosed BL height (black line) (see 2.32.3.2).

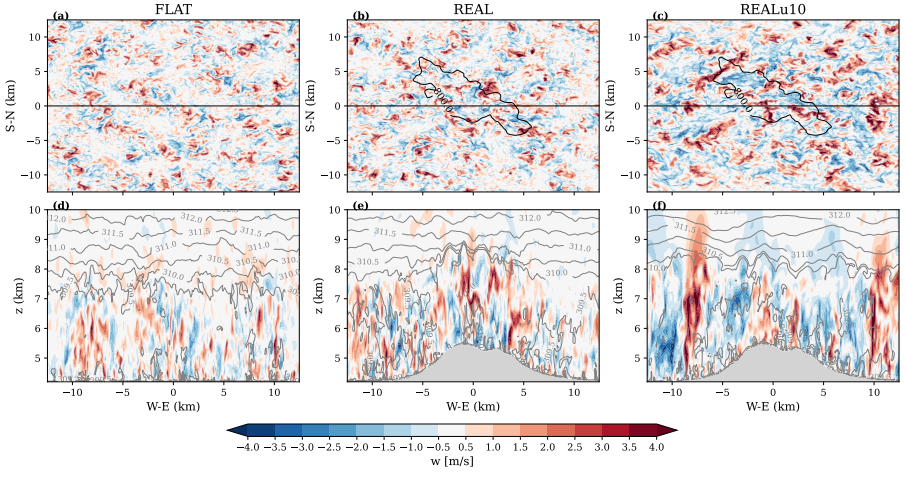

Figure 4. As in Fig. 3, but for instantaneous turbulent flow fields of vertical velocity perturbations w' (shaded), and instantaneous θ' (gray contours).

adjacent to mountainous regions. In stark contrast is REALu10 (Fig. 3c,f), where convection results in elongated slanted streaks in the direction of the mean wind. These streaks reflect the formation of roll-like vortices, a property of shear-dominated turbulent boundary layers. The result is a transition from isolated stationary updrafts to a more continuous, shear-aligned convection structure. The updrafts seen in the vertical cross-section are slanted and lower in magnitude, which implies reduced stationarity.

https://doi.org/10.5194/egusphere-2025-4302
Preprint. Discussion started: 17 September 2025

3.2 Instantaneous Flow Patterns

Figure 4 presents the instantaneous flow fields of vertical velocity perturbations and potential temperature at 15 LT. The simulations share identical surface sensible heat fluxes and initial conditions, which leads to broadly similar turbulent structures across all cases. In the horizontal cross-sections (Fig.4, top) the turbulent field exhibits an irregular cellular pattern, with eddy diameters ranging from a few hundred meters to over 2 km. In FLAT, eddies are more or less randomly distributed throughout the domain, consistent with the homogeneous surface. In contrast, both REAL and REALu10 display clustering of eddies above elevated terrain, suggesting enhanced organization driven by the underlying orographic features. In the vertical cross-sections for REAL and REALu10 (Fig. 4, bottom) large, energy-containing eddies penetrate into the overlying weakly stable layer, particularly over elevated terrain in REAL, as well as above flatter regions in REALu10, indicating stronger vertical momentum transport in the presence of terrain-modulated wind shear.

In addition to horizontal sections shown in Fig. 4, we examined instantaneous vertical velocity perturbation fields at lower levels (not shown). At these heights (e.g., 500 m AGL), the turbulent structures appear as irregular, fine-scale cells, reflecting the direct influence of surface heating and frictional turbulence. They are in contrast to the flow at 1800 m AGL, which has larger, more coherent eddies and characteristic of fully developed convection.

3.3 Turbulence and Mixing

We examine turbulence intensity in terms of turbulence kinetic energy (TKE),

$$\mathrm{TKE} = \frac{1}{2}\overline{(u'^2 + v'^2 + w'^2)}, \tag{3}$$

where u'^2, v'^2, w'^2 are the difference between the time-averaged second and first moments:

$$w'^2 = \tilde{u^{2t}} - (\tilde{u}^t)^2 \tag{4}$$

$$w'^2 = \tilde{v^{2t}} - (\tilde{v}^t)^2 \tag{5}$$

$$w'^2 = \tilde{w^{2t}} - (\tilde{w}^t)^2 \tag{6}$$

During the day, vigorous turbulence efficiently mixes heat, momentum, and scalars, producing a well-developed CBL. At midday (15 LT), the TKE profiles of FLAT and REAL are similar, while REALu10 exhibits systematically higher values throughout and above the ABL (Fig. 5). Since all runs start from identical conditions, this enhancement is expected: the added wind shear in REALu10 directly contributes to turbulence production. Shear also organizes turbulence into roll structures, in contrast to the isolated plumes seen in the no-shear cases (REAL and FLAT) (Fig. 6a–c).

Between 15 LT and 19 LT, turbulence intensifies and convective eddies deepen in all experiments (Fig. 6d–f). By 19 LT, each case shows a very deep, well-mixed boundary layer, though an important distinction emerges: rather than decaying, TKE remains high into the evening, particularly in REALu10. This persistence contrasts with the typical late-afternoon decline expected as surface fluxes weaken (Stull, 1988), and points to sustained thermally driven circulations under weak upper-level stability, consistent with the atmospheric structure reported by Chen et al. (2016).

https://doi.org/10.5194/egusphere-2025-4302
Preprint. Discussion started: 17 September 2025

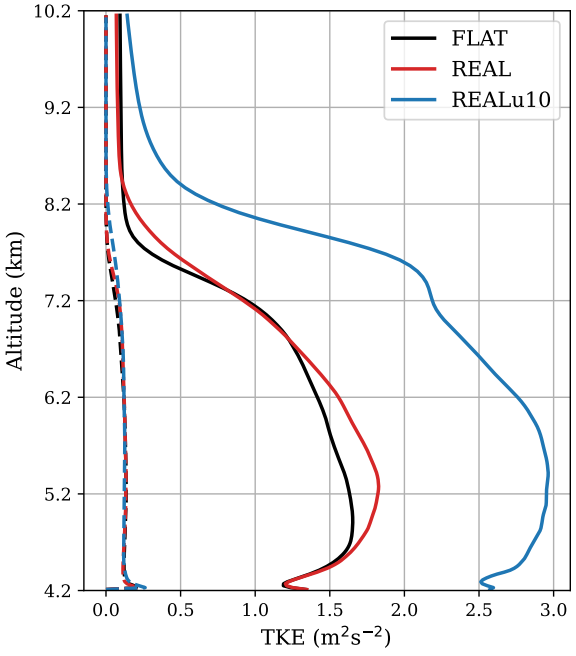

Figure 5. Mean vertical profile of resolved TKE (solid lines) at 15 LT on the interpolated horizontal surfaces. The dashed lines represent subgrid TKE.

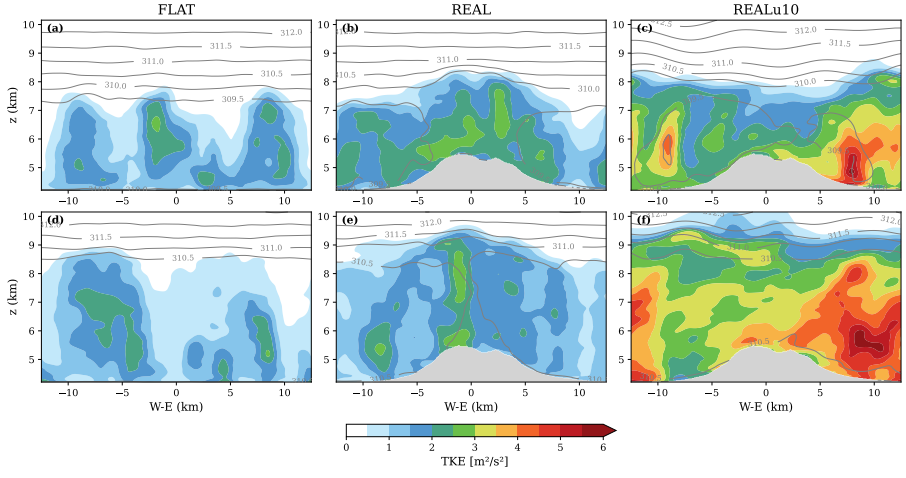

Figure 6. Vertical cross-sections of resolved TKE at 15 LT (a-c) and 19 LT (d-f), with $\overline{\theta}$ in gray contours.

https://doi.org/10.5194/egusphere-2025-4302
Preprint. Discussion started: 17 September 2025

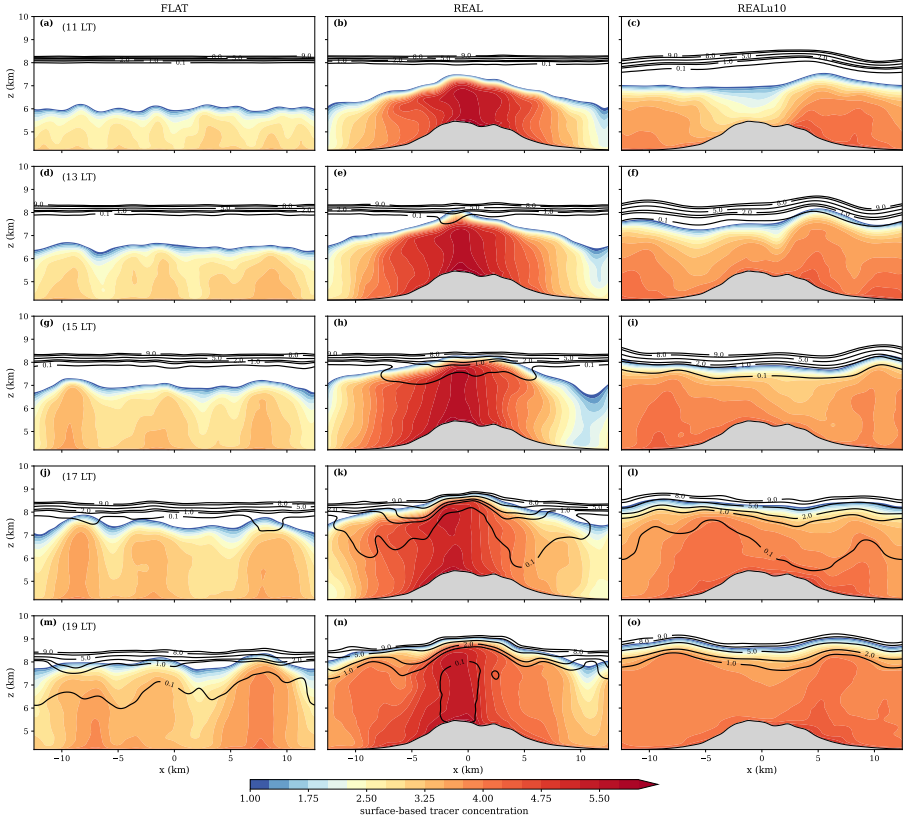

Figure 7. Vertical cross-sections of the ensemble average surface-based (shaded) and upper-level (black contours) passive tracers for the FLAT (left), REAL (middle), and REALu10 (right column) experiments, shown from 11-19 LT times throughout the simulation (rows). Shading for the surface-based tracer is applied above 10% of the mean ABL tracer concentration to emphasize distinctive features.

Terrain plays a clear role in shaping turbulence. In FLAT, TKE exhibits the classic CBL structure, with maxima concentrated in the mid-to-upper mixed layer, reflecting homogeneous surface forcing. In REAL, terrain heterogeneity enhances mixed-layer turbulence and anchors convective eddies to slopes, producing a more continuous turbulent layer that extends above 9 km ASL by 19 LT. The combined effects of terrain forcing and added shear in REALu10 further amplify turbulence and promote vertical TKE growth.

3.4 Passive Tracers and ABL height Diagnosis

By midday, convective turbulence mixes surface tracers within the growing boundary layer, producing a well-mixed state (Fig. 7). Columns of elevated tracer concentration coincide with persistent updraft cores (Fig. 3), especially over complex terrain where stationary thermals continuously draw tracers upward. In REAL, these terrain-anchored plumes generate localized

https://doi.org/10.5194/egusphere-2025-4302
Preprint. Discussion started: 17 September 2025

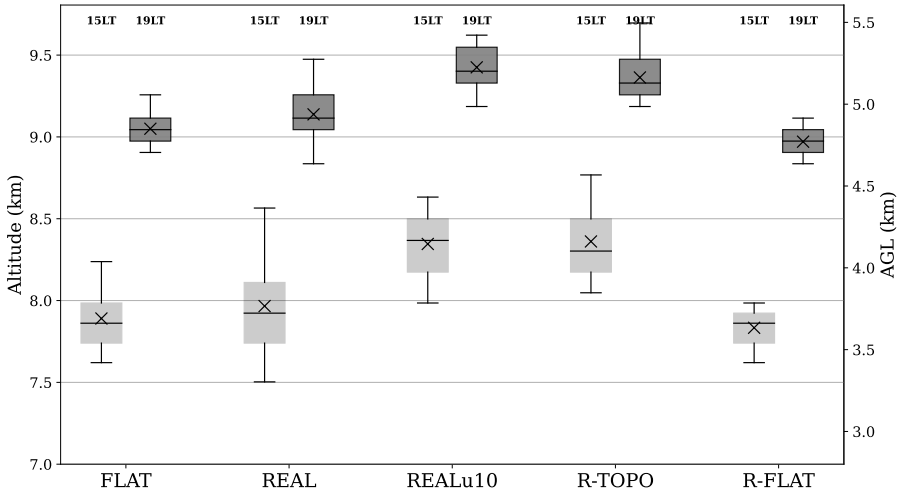

Figure 8. Horizontal distributions of ensemble average surface-based tracer concentration (y-axis) for each experiment and subdomain (x-axis), shown at 15 LT (light gray boxes) and 19 LT (dark gray boxes). The boxes represent the interquartile range (25th–75th percentiles), with the median shown as a horizontal line and whiskers extending to the 5th and 95th percentiles. The mean concentration is marked with an "×" symbol.

tracer maxima and uneven mixing, whereas in REALu10 the added shear produces more homogeneous horizontal tracer fields and shear-organized rolls (Fig. 6), leading to more uniform mixing.

The vertical tracer extent provides a clear marker of mixing depth, closely corresponding to turbulence maxima (Fig. 6) and thermal perturbations (Fig. 4). In REAL, tracer and turbulence extend higher over the ridge, while in REALu10 the tracer reaches greater heights over adjacent flat areas, consistent with shear-enhanced mixing. Entrainment from aloft further highlights these differences: in REAL, upper-level tracer mixes downward by 15 LT along the mountain flanks, whereas in FLAT entrainment is delayed until 17–19 LT and occurs sporadically with random downdrafts. REALu10 achieves domain-wide, uniform entrainment, and by 19 LT exhibits a gentle wave-like pattern with minima over the ridge and maxima over the plains. The total entrained tracer by late afternoon is smallest in FLAT, while REAL and REALu10 reach comparable totals but with distinct spatial distributions.

Tracer-based profiles and diagnosed ABL heights (Figs. 8) confirm these contrasts. At 15 LT, surface tracer concentrations are highest in the mountainous R-TOPO subdomain and lowest in FLAT, with intermediate values elsewhere. The corresponding ABL height distributions reflect this: REAL and R-TOPO are right-skewed with large variability, while FLAT and R-FLAT are narrow and symmetric, consistent with the absence of stationary thermals. By 19 LT, all cases develop very deep ABLs (9 km ASL) and the distributions become more symmetric as convective mixing homogenizes.

Quantitatively, at 15 LT the mean ABL height in R-TOPO exceeds R-FLAT by 534 m (14.8%), and by 19 LT the difference remains 397 m (8.3%) (Table 2). Wind shear further amplifies mixing: compared to REAL, the mean ABL height in REALu10 is higher by 383 m at 15 LT and 288 m at 19 LT. Thus, terrain-anchored thermals act as persistent pumps that deepen the

https://doi.org/10.5194/egusphere-2025-4302
Preprint. Discussion started: 17 September 2025

Table 2. Differences in diagnosed mean ABL height between experiments at 15 LT and 19 LT. The values indicate the absolute difference in meters, with the relative difference of the absolute ABL height (AGL) in parentheses.

Comparison	15 LT	19 LT
REAL / FLAT	77 m (2.1%)	88 m (1.8%)
R-TOPO / R-FLAT	534 m (14.8%)	397 m (8.3%)
REALu10 / REAL	383 m (10.2%)	288 m (5.9%)
REALu10 / FLAT	459 m (12.6%)	377 m (7.8%)

boundary layer locally, while shear-driven rolls mix efficiently across the domain. Their combined effects are roughly additive (in Table 2: REAL/FLAT + REALu10/REAL), yielding both a deeper and more laterally uniform ABL.

On the other hand, the comparison between REAL and FLAT shows only a small difference in the mean ABL height (∼80–90 m; Table 2). However, mean values mask the upper-tail behaviour: when considering higher percentiles (75th–95th), the differences become much more pronounced. These upper percentiles are particularly relevant for transport into the upper troposphere–lower stratosphere region, since the deepest convective columns are responsible for mixing upper-level tracer downward. In our simulations, the 75th–95th percentile differences range from 110–330 m (3–8%) for REAL/FLAT and from 550–770 m (11–20%) for R-TOPO/R-FLAT (not shown).

Finally, our tracer-based ABL height detection method (Section 2.3.2) proved robust: applying a 5% concentration threshold yielded consistent and physically meaningful height distributions that aligned well with turbulence features (Fig. 6). Importantly, similar distributions were obtained whether using instantaneous fields, time-averaged data, or ensemble means, indicating that the method is not overly sensitive to the choice of averaging. Together, these diagnostics confirm that small-scale orography and wind shear jointly control vertical mixing, entrainment, and the structure of the deep CBL.

4 Conclusions

In this study, we performed high-resolution LES experiments under idealized dry conditions to quantify the impact of small-scale orography on the development of a deep CBL over the western Tibetan Plateau. We compared simulations with realistic complex terrain (REAL) (an isolated mountain) versus a flat surface (FLAT) (both at 4.2 km elevation). The two cases are without any background wind, and one case with a steady upper-level winds, to isolate the effects of orography and wind shear (REALu10). Small-scale orography enhanced early afternoon boundary layer growth, with ABL heights over mountain ridges exceeding nearby flat areas by up to 534 m (15 LT, ∼15%) and 397 m (19 LT, ∼8%). Adding a steady background wind of 10 m s^{-1} further deepened the boundary layer: REALu10 exceeded REAL by 383 m (15 LT, ∼10%) and 288 m (19 LT, ∼6%), yielding the deepest and most laterally uniform ABL by late afternoon (∼9.4 km ASL). These terrain and shear effects were approximately additive. In addition, terrain anchored convective updrafts that intensified TKE and tracer plumes over the ridge, while shear organized turbulence into roll vortices that homogenized mixing across the domain. Together,

https://doi.org/10.5194/egusphere-2025-4302
Preprint. Discussion started: 17 September 2025

these results demonstrate that small-scale orography and shear act through distinct but complementary mechanisms: terrain-induced thermals create localized deep plumes and accelerate entrainment along slopes and ridges, while shear-driven rolls enhance domain-wide mixing efficiency. Their combined action promotes both earlier entrainment of free-tropospheric tracer and deeper afternoon boundary layers than flat, no-shear conditions.

The extreme ABL depths reproduced in our simulations are consistent with radiosonde observations over the Tibetan Plateau, which report CBLs of up to 5 km AGL (∼9.4 km ASL) under fair-weather winter conditions (Chen et al., 2013, 2016). Our results reinforce the importance of weak stratification aloft and strong surface heating as prerequisites for such development. Upper-level tracer entrainment also aligns with observed pathways for stratospheric ozone to influence surface air (Yin et al., 2023), and the contrasting tracer distributions between REAL and REALu10 are consistent with terrain-anchored plumes and shear-driven rolls identified in earlier modeling studies (Lai et al., 2021). These findings support growing evidence that unresolved orography biases ABL representation and that explicitly resolving terrain circulations improves realism (Wagner et al., 2014; Guo et al., 2021; Poll et al., 2022; Goger et al., 2022).

Our setup is intentionally idealized, excluding moist convection, clouds, and synoptic variability, in order to isolate terrain effects. This design strengthens attribution but also limits direct comparability with real cases. The robustness of our conclusions should be tested in future work with real-case forcing (e.g., TIPEX-III field days; (Che and Zhao, 2021)) and through sensitivity experiments that vary stability and background flow (cf. Singh et al., 2024). Such extensions will help assess the generality of these processes under more complex atmospheric states.

Overall, our results show that small-scale orography sustains and organizes turbulence over the Tibetan Plateau, thereby enhancing boundary-layer mixing and contributing to the exceptionally deep ABLs that form under weak free-tropospheric stability during springtime. These terrain-driven processes are subgrid-scale in most weather and climate models and therefore remain unresolved, yet they exert a decisive influence on boundary-layer depth and mixing. Better representation of these mechanisms is essential for simulating vertical transport of heat, momentum, and trace species, and for improving forecasts and climate projections in mountainous environments.

Code and data availability. The tarrain data is open-access and is available at https://usgs.gov/centers/eros/science/usgs-eros-archive-digital-elevation-shuttle-radar-topography-mission-srtm-1. The CM1 model is open-access and is available at https://www2.mmm.ucar.edu/people/bryan/cm1/ (Bryan and Fritsch, 2002). The raw LES data used in this study, as well as TKE data and the Python code used to produce the figures for the manuscript, is openly available at https://doi.org/10.5281/zenodo.17093768 (Basic & Jadhav, 2025).

Appendix A: Comparison Between Two ABL height Diagnosis Methods

To evaluate the robustness of our tracer-based boundary layer height (ABL height) diagnosis, we compare it against a commonly used alternative: the parcel method (Duncan Jr. et al., 2022).

https://doi.org/10.5194/egusphere-2025-4302
Preprint. Discussion started: 17 September 2025

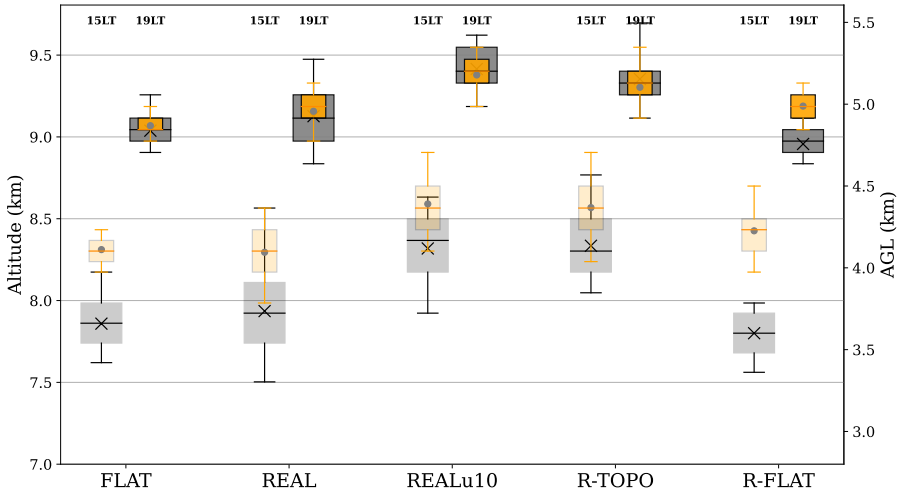

Figure A1. As in Fig. 8, but comparing the tracer ABL height to the parcel ABL height method at 15 LT (light orange boxes) and 19 LT (dark orange boxes). The mean parcel ABL height is marked with an "o" symbol.

The TKE threshold method was initially considered, but ultimately excluded from the analysis. It exhibited high spatial and temporal variability and required sensitive tuning of threshold values. Despite such tuning efforts, it consistently produced less physically plausible results compared to the parcel method and tracer-based approach.

Figure A1 shows a comparison between the tracer-based ABL height and the parcel ABL height at 15 and 19 LT, with the parcel method using ensemble averaged potential temperatures ($\overline{\theta}$). The parcel method diagnoses the median and mean ABL height values exceed those from the tracer method by a substantial margin at 15 LT (apart from REALu10 and R-TOPO). While the initial rise is faster, the ABL heights at 19 LT are comparable. The differences between the distributions of ABL heights between the experiments are lesser in the parcel method (see Table A1), than in the tracer method (Table 2). On a closer look, it could be due to the ABL height at 09 LT being almost 1 km higher than in the tracer method, since the surface passive tracer starts at zero. The difference between FLAT and REAL are non-existent at 15 LT, but are higher than one in the tracer method at 19 LT.

The tracer method we used better captures the integrated effects of turbulent mixing and entrainment and avoids overestimation in regions with strong surface heterogeneity. While it does not capture sharp inversion layers as directly as temperature-based methods, its stability and sensitivity to vertical transport make it well-suited for diagnosing the evolving CBL in high-altitude terrain.

Author contributions. IB: Conceptualization, Methodology, Software, Formal analysis, Writing – original draft, Writing – review & editing. HJ: Visualization, Software, Data curation, Writing – review & editing. JS: Supervision, Project administration, Writing – review & editing. JS (Singh): Supervision, Writing – review & editing.

https://doi.org/10.5194/egusphere-2025-4302
Preprint. Discussion started: 17 September 2025

Table A1. As in Table 2, but for ABL heights diagnosed with the parcel method.

Comparison	15 LT	19 LT
REAL / FLAT	0 m (0.0%)	141 m (2.9%)
R-TOPO / R-FLAT	132 m (3.1%)	143 m (2.9%)
REALu10 / REAL	263 m (6.4%)	216 m (4.3%)
REALu10 / FLAT	263 m (6.4%)	357 m (7.4%)

Competing interests. The authors declare that they have no conflict of interest.

Acknowledgements. This work used resources of the Deutsches Klimarechenzentrum (DKRZ), granted by its Scientific Steering Committee (WLA) under project ID bb1096. The research was funded by the Deutsche Forschungsgemeinschaft (DFG, German Research Foundation) – TRR 301 – Project-ID 428312742, and by the Federal Office of Meteorology and Climatology MeteoSwiss within the framework of GAW-CH. This research was supported by the Hans-Ertel-Centre for Weather Research, funded by the German Federal Ministry for Transportation and Digital Infrastructure (Grant 4823DWDP3). The author used AI tools (OpenAI) to enhance manuscript fluency, spot repetition, and to correct grammar.

https://doi.org/10.5194/egusphere-2025-4302
Preprint. Discussion started: 17 September 2025

References

Borges, R., Carmona, M., Costa, B., and Don, W. S.: An improved weighted essentially non-oscillatory scheme for hyperbolic conservation laws, Journal of Computational Physics, 227, 3191–3211, https://doi.org/10.1016/j.jcp.2007.11.038, 2008.

Bryan, G. H. and Fritsch, J. M.: A Benchmark Simulation for Moist Nonhydrostatic Numerical Models, Monthly Weather Review, 130, 2917–2928, https://doi.org/10.1175/1520-0493(2002)130<2917:ABSFMN>2.0.CO;2, 2002.

Che, J. and Zhao, P.: Characteristics of the summer atmospheric boundary layer height over the Tibetan Plateau and influential factors, Atmospheric Chemistry and Physics, 21, 5253–5268, https://doi.org/10.5194/acp-21-5253-2021, 2021.

Chen, X., Añel, J. A., Su, Z., De La Torre, L., Kelder, H., Van Peet, J., and Ma, Y.: The Deep Atmospheric Boundary Layer and Its Significance to the Stratosphere and Troposphere Exchange over the Tibetan Plateau, PLoS ONE, 8, e56 909, https://doi.org/10.1371/journal.pone.0056909, publisher: Public Library of Science (PLoS), 2013.

Chen, X., Škerlak, B., Rotach, M. W., Añel, J. A., Su, Z., Ma, Y., and Li, M.: Reasons for the Extremely High-Ranging Planetary Boundary Layer over the Western Tibetan Plateau in Winter, Journal of the Atmospheric Sciences, 73, 2021–2038, https://doi.org/10.1175/JAS-D-15-0148.1, 2016.

Deardorff, J. W.: Stratocumulus-capped mixed layers derived from a three-dimensional model, Boundary-Layer Meteorology, 18, 495–527, https://doi.org/10.1007/BF00119502, 1980.

Duncan Jr., J. B., Bianco, L., Adler, B., Bell, T., Djalalova, I. V., Riihimaki, L., Sedlar, J., Smith, E. N., Turner, D. D., Wagner, T. J., and Wilczak, J. M.: Evaluating convective planetary boundary layer height estimations resolved by both active and passive remote sensing instruments during the CHEESEHEAD19 field campaign, Atmospheric Measurement Techniques, 15, 2479–2502, https://doi.org/10.5194/amt-15-2479-2022, publisher: Copernicus GmbH, 2022.

Gerken, T., Babel, W., Herzog, M., Fuchs, K., Sun, F., Ma, Y., Foken, T., and Graf, H.-F.: High-resolution modelling of interactions between soil moisture and convective development in a mountain enclosed Tibetan Basin, Hydrology and Earth System Sciences, 19, 4023–4040, https://doi.org/10.5194/hess-19-4023-2015, 2015.

Goger, B., Stiperski, I., Nicholson, L., and Sauter, T.: Large-eddy simulations of the atmospheric boundary layer over an Alpine glacier: Impact of synoptic flow direction and governing processes, Quarterly Journal of the Royal Meteorological Society, 148, 1319–1343, https://doi.org/10.1002/qj.4263, 2022.

Guo, J., Zhang, J., Yang, K., Liao, H., Zhang, S., Huang, K., Lv, Y., Shao, J., Yu, T., Tong, B., Li, J., Su, T., Yim, S. H. L., Stoffelen, A., Zhai, P., and Xu, X.: Investigation of near-global daytime boundary layer height using high-resolution radiosondes: first results and comparison with ERA5, MERRA-2, JRA-55, and NCEP-2 reanalyses, Atmospheric Chemistry and Physics, 21, 17 079–17 097, https://doi.org/10.5194/acp-21-17079-2021, publisher: Copernicus GmbH, 2021.

Jiang, G.-S. and Shu, C.-W.: Efficient Implementation of Weighted ENO Schemes, Journal of Computational Physics, 126, 202–228, https://doi.org/10.1006/jcph.1996.0130, 1996.

Klemp, J. B. and Wilhelmson, R. B.: The Simulation of Three-Dimensional Convective Storm Dynamics, Journal of Atmospheric Sciences, 35, 1070 – 1096, https://doi.org/10.1175/1520-0469(1978)035<1070:TSOTDC>2.0.CO;2, 1978.

Lai, Y., Chen, X., Ma, Y., Chen, D., and Zhaxi, S.: Impacts of the Westerlies on Planetary Boundary Layer Growth Over a Valley on the North Side of the Central Himalayas, Journal of Geophysical Research: Atmospheres, 126, e2020JD033 928, https://doi.org/10.1029/2020JD033928, 2021.

https://doi.org/10.5194/egusphere-2025-4302
Preprint. Discussion started: 17 September 2025

Lehner, M. and Rotach, M.: Current Challenges in Understanding and Predicting Transport and Exchange in the Atmosphere over Mountainous Terrain, Atmosphere, 9, 276, https://doi.org/10.3390/atmos9070276, 2018.

Li, Y. and Gao, W.: Atmospheric Boundary Layer Circulation on the Eastern Edge of the Tibetan Plateau, China, in Summer, Arctic, Antarctic, and Alpine Research, 39, 708–713, https://doi.org/10.1657/1523-0430(07-504)[LI]2.0.CO;2, 2007.

Mulholland, J. P., Peters, J. M., and Morrison, H.: How Does LCL Height Influence Deep Convective Updraft Width?, Geophysical Research Letters, 48, e2021GL093 316, https://doi.org/10.1029/2021GL093316, 2021.

Ojha, N., Pozzer, A., Akritidis, D., and Lelieveld, J.: Secondary ozone peaks in the troposphere over the Himalayas, Atmospheric Chemistry and Physics, 17, 6743–6757, https://doi.org/10.5194/acp-17-6743-2017, 2017.

Poll, S., Shrestha, P., and Simmer, C.: Grid resolution dependency of land surface heterogeneity effects on boundary-layer structure, Quarterly Journal of the Royal Meteorological Society, 148, 141–158, https://doi.org/10.1002/qj.4196, 2022.

Rajput, A., Singh, N., Singh, J., and Rastogi, S.: Investigation of atmospheric turbulence and scale lengths using radiosonde measurements of GVAX-campaign over central Himalayan region, Journal of Atmospheric and Solar-Terrestrial Physics, 235, 105 895, https://doi.org/10.1016/j.jastp.2022.105895, 2022.

Santanello, J. A., Friedl, M. A., and Kustas, W. P.: An Empirical Investigation of Convective Planetary Boundary Layer Evolution and Its Relationship with the Land Surface, Journal of Applied Meteorology, 44, 917–932, https://doi.org/10.1175/jam2240.1, publisher: American Meteorological Society, 2005.

Serafin, S., Adler, B., Cuxart, J., De Wekker, S., Gohm, A., Grisogono, B., Kalthoff, N., Kirshbaum, D., Rotach, M., Schmidli, J., Stiperski, I., Večenaj, v., and Zardi, D.: Exchange Processes in the Atmospheric Boundary Layer Over Mountainous Terrain, Atmosphere, 9, 102, https://doi.org/10.3390/atmos9030102, 2018.

Singh, J., Singh, N., Ojha, N., Sharma, A., Pozzer, A., Kiran Kumar, N., Rajeev, K., Gunthe, S. S., and Kotamarthi, V. R.: Effects of spatial resolution on WRF v3.8.1 simulated meteorology over the central Himalaya, Geoscientific Model Development, 14, 1427–1443, https://doi.org/10.5194/gmd-14-1427-2021, 2021.

Singh, J., Singh, N., Ojha, N., Dimri, A., and Singh, R. S.: Impacts of different boundary layer parameterization schemes on simulation of meteorology over Himalaya, Atmospheric Research, 298, 107 154, https://doi.org/10.1016/j.atmosres.2023.107154, 2024.

Singh, N., Solanki, R., Ojha, N., Janssen, R. H. H., Pozzer, A., and Dhaka, S. K.: Boundary layer evolution over the central Himalayas from radio wind profilerand model simulations, Atmospheric Chemistry and Physics, 16, 10 559–10 572, https://doi.org/10.5194/acp-16-10559-2016, 2016.

Slättberg, N., Lai, H., Chen, X., Ma, Y., and Chen, D.: Spatial and temporal patterns of planetary boundary layer height during 1979–2018 over the Tibetan Plateau using ERA5, International Journal of Climatology, 42, 3360–3377, https://doi.org/10.1002/joc.7420, 2022.

Solanki, R., Singh, N., Kiran Kumar, N. V. P., Rajeev, K., Imasu, R., and Dhaka, S. K.: Impact of Mountainous Topography on Surface-Layer Parameters During Weak Mean-Flow Conditions, Boundary-Layer Meteorology, 172, 133–148, https://doi.org/10.1007/s10546-019-00438-3, 2019.

Stull, R. B.: An introduction to boundary layer meteorology, Meteorology, Kluwer Academic Publishers, P.O. Box 17, 3300 AA Dordrecht, The Netherlands, 1st edn., ISBN 978-90-277-2769-5, 1988.

U.S. Geological Survey: Shuttle Radar Topography Mission (SRTM) 1 Arc-Second Global, https://usgs.gov/centers/eros/science/usgs-eros-archive-digital-elevation-shuttle-radar-topography-mission-srtm-1, accessed: 2025-06-27, 2015.

https://doi.org/10.5194/egusphere-2025-4302
Preprint. Discussion started: 17 September 2025

Wagner, J. S., Gohm, A., and Rotach, M. W.: The Impact of Horizontal Model Grid Resolution on the Boundary Layer Structure over an Idealized Valley, Monthly Weather Review, 142, 3446–3465, https://doi.org/10.1175/MWR-D-14-00002.1, 2014.

Weinkaemmerer, J., Ďurán, I. B., and Schmidli, J.: The Impact of Large-Scale Winds on Boundary Layer Structure, Thermally Driven Flows, and Exchange Processes over Mountainous Terrain, Journal of the Atmospheric Sciences, 79, 2685–2701, https://doi.org/10.1175/JAS-D-21-0195.1, 2022.

Xu, Z., Chen, H., Guo, J., and Zhang, W.: Contrasting Effect of Soil Moisture on the Daytime Boundary Layer Under Different Thermodynamic Conditions in Summer Over China, Geophysical Research Letters, 48, https://doi.org/10.1029/2020gl090989, publisher: American Geophysical Union (AGU), 2021.

Yin, X., Rupakheti, D., Zhang, G., Luo, J., Kang, S., De Foy, B., Yang, J., Ji, Z., Cong, Z., Rupakheti, M., Li, P., Hu, Y., and Zhang, Q.: Surface ozone over the Tibetan Plateau controlled by stratospheric intrusion, Atmospheric Chemistry and Physics, 23, 10 137–10 143, https://doi.org/10.5194/acp-23-10137-2023, 2023.

Zhang, Q., Zhang, J., Qiao, J., and Wang, S.: Relationship of atmospheric boundary layer depth with thermodynamic processes at the land surface in arid regions of China, Science China Earth Sciences, 54, 1586–1594, https://doi.org/10.1007/s11430-011-4207-0, publisher: Springer Science and Business Media LLC, 2011.

Zhang, Y., Huang, Q., Ma, Y., Luo, J., Wang, C., Li, Z., and Chou, Y.: Large eddy simulation of boundary-layer turbulence over the heterogeneous surface in the source region of the Yellow River, Atmospheric Chemistry and Physics, 21, 15 949–15 968, https://doi.org/10.5194/acp-21-15949-2021, 2021.

Zhao, C., Meng, X., Zhao, L., Guo, J., Li, Y., Liu, H., Li, Z., Han, B., and Lyu, S.: Energy Mechanism of Atmospheric Boundary Layer Development Over the Tibetan Plateau, Journal of Geophysical Research: Atmospheres, 128, e2022JD037 332, https://doi.org/10.1029/2022JD037332, 2023.